

This is the accepted manuscript made available via CHORUS. The article has been published as:

Fragile morphotropic phase boundary and phase stability in the near-surface region of the relaxor ferroelectric $(1-x)\text{Pb}(\text{Zn}_{1/3}\text{Nb}_{2/3})\text{O}_3-x\text{PbTiO}_3$: [001] field-cooled phase diagrams

Yaojin Wang (✉), Ding Wang, Guoliang Yuan, He Ma, Feng Xu, Jiefang Li, D. Viehland, and Peter M. Gehring

Phys. Rev. B **94**, 174103 — Published 10 November 2016

DOI: [10.1103/PhysRevB.94.174103](https://doi.org/10.1103/PhysRevB.94.174103)

1 **Fragile morphotropic phase boundary and phase stability in the near-surface**
2 **region of relaxor ferroelectric $\text{Pb}(\text{Zn}_{1/3}\text{Nb}_{2/3})\text{O}_3\text{-xPbTiO}_3$: [001] field-cooled phase**
3 **diagrams**

4 Yaojin Wang (汪尧进)^{1,2,a}, Ding Wang¹, Guoliang Yuan¹, He Ma¹, Feng Xu¹, Jiefang
5 Li², D. Viehland², Peter M. Gehring³

6 ¹ *School of Materials Science and Engineering, Nanjing University of Science and Technology,*
7 *Nanjing 210094, Jiangsu, China*

8 ² *Materials Science and Engineering, Virginia Tech, Blacksburg, Virginia 24061, USA*

9 ³ *NIST Center for Neutron Research, National Institute of Standards and Technology,*
10 *Gaithersburg, MD 20899-6100, USA*

11 We have examined the effects of field cooling on the phase diagram of the relaxor system
12 $(1-x)\text{Pb}(\text{Zn}_{1/3}\text{Nb}_{2/3})\text{O}_3\text{-xPbTiO}_3$ (PZN-xPT) for compositions near the morphotropic phase
13 boundary (MPB). High-resolution diffraction measurements using Cu K_α x-rays, which probe \approx
14 $3\ \mu\text{m}$ below the crystal surface, were made on field-cooled (FC) single crystal specimens of
15 PZN-4.5%PT and PZN-6.5%PT under electric fields of 1 kV/cm and 2 kV/cm applied along
16 [001] and combined with previous neutron diffraction data, which probe the entire crystal
17 volume for FC PZN-8%PT [Ohwada *et al.*, Phys. Rev. B **67**, 094111 (2003)]. A comparison to
18 the zero-field-cooled (ZFC) PZN-xPT phase diagram reveals several interesting features: (1) the
19 short-range monoclinic phase observed in the ZFC state on the low-PT side of the MPB is
20 replaced by a monoclinic M_A phase; (2) field cooling extends the tetragonal (T) phase to higher
21 temperatures and lower-PT concentrations on field cooling; (3) the orthorhombic (O) phase near
22 the MPB is replaced by a monoclinic M_C phase; (4) the vertical MPB in the ZFC phase diagram
23 bends significantly towards the low-PT side in the FC state. These results demonstrate that both

24 the phase stability and the nature of the MPB in PZN-PT within the near-surface regions are
25 fragile in the presence of electric fields.

26 ^{a)} Electronic mail: yiwang@njust.edu.cn

27 I. INTRODUCTION

28 Piezoelectrics are materials that convert mechanical energy to electrical energy and vice-
29 versa. They are thus of significant importance to medical ultrasound, actuators, sensors, and
30 countless other device applications¹⁻³. Amongst such materials, solid solutions of the complex
31 perovskites $\text{Pb}(\text{Zn}_{1/3}\text{Nb}_{2/3})\text{O}_3$ and $\text{Pb}(\text{Mg}_{1/3}\text{Nb}_{2/3})\text{O}_3$ with PbTiO_3 (denoted PZN-xPT and PMN-
32 xPT, respectively, where x indicates the atomic percentage of Ti) are relaxor ferroelectrics that
33 exhibit exceptional piezoelectric properties². In particular, extraordinarily high values of the
34 longitudinal piezoelectric coefficient d_{33} have been reported for PZN-8%PT when an electric
35 field (E) is applied along the pseudocubic [001] direction, reaching values of 2500 pC/N and
36 induced strains $\varepsilon \geq 1.7\%$ ^{2,4}. These values are nearly one order of magnitude larger than those
37 observed for conventional piezoelectric ceramics such as $\text{Pb}(\text{Zr}_x\text{Ti}_{1-x})\text{O}_3$ (PZT). Yet PMN-xPT,
38 PZN-xPT, and PZT have qualitatively similar temperature-composition phase diagrams: the
39 high-temperature paraelectric phases are all cubic (C – space group $Pm3m$), and the low-
40 temperature ferroelectric phases are rhombohedral (R – space group $R3m$) for low x and
41 tetragonal (T – space group $P4mm$) at higher x⁵⁻⁷. The strong piezoelectric properties of these
42 materials have been associated with a very steep morphotropic phase boundary (MPB) that
43 separates the T and R phases^{5,6,8}. For this reason, many diffraction studies have been performed
44 with excellent wave vector (q) resolution to try to identify the low-symmetry phase located
45 closest to the MPB on the rhombohedral side and to determine the extent of its stability.

46 In PZT, monoclinic $Cm A$ (M_A) and $Cm B$ (M_B) phases have been reported that bridge the R
47 and T phases near the MPB for $0.46 \leq x \leq 0.52$ ⁹⁻¹¹. The M_A and M_B phases have a unique axis b_m
48 that lies along the $[110]$ direction; the unit cell is doubled and rotated 45° about the c -axis with
49 respect to the primitive C cell¹². In PMN-xPT, however, the MPB region is also complicated.
50 Monoclinic $Pm C$ (M_C) and M_B phases coexist with R , T , and orthorhombic $Amm2$ (O) phases
51 for $0.30 \leq x \leq 0.37$ ^{5,13}. The M_C phase has a primitive unit cell, with a unique axis b_m oriented along
52 $[010]$. For PZN-xPT, the existence of an O phase over a narrow composition region ($0.09 \leq x$
53 ≤ 0.11) has been reported between the R and T phases⁶. The O phase in $BaTiO_3$ can be viewed as
54 a limiting case of the monoclinic M_C phase with $a_m = c_m$ ¹⁴. Uesu *et al.* also observed an M_C phase
55 (i.e., $a_m \neq c_m$) in the ground state of one PZN-9%PT crystal, however two others exhibited a
56 stable O phase¹⁵. Since the seminal discovery of an intermediate monoclinic phase in PZT^{10,16},
57 the zero-field-cooled (ZFC) temperature-composition phase diagrams of these other lead-oxide
58 perovskite ferroelectric relaxors have been revised^{5,6,10,11,13}.

59 Generally, an applied electric field (E) will alter the free-energy landscape and thus the
60 various possible polar phases in the vicinity of the MPB¹⁷. Recently, Tan *et al.*¹⁸ reported that
61 the MPB of annealed, lead-free $(Bi_{1/2}Na_{1/2})TiO_3$ - $BaTiO_3$ can be created, destroyed, or even
62 replaced by another MPB, via phase transitions induced by poling. Moreover, Cao *et al.*¹⁹ have
63 constructed field-cooled (FC) temperature-composition phase diagrams for PMN-xPT for E
64 applied parallel to $[001]$ and $[110]$. These FC diagrams revealed two interesting features: (i) the
65 presence of a pseudocubic region of abnormal thermal expansion ($c \neq a$) above the dielectric
66 maximum, where the stability range extends to higher temperatures than in the ZFC state; and
67 (ii) a change in the shape of the MPB in the FC state, i.e., the stability of the T phase is extended
68 to $x=0.25$ in the $[001]$ FC state, and it is replaced by an O phase in the $[110]$ FC state¹⁹. For

69 PZN-8%PT, Ohwada *et al.*²⁰ reported the phase transition sequence $C \rightarrow T \rightarrow M_C$ on cooling from
70 550 K to 300 K in an electric field $E // [001]$. Compared with the ZFC diagram⁶, it was found
71 that the $C \rightarrow T$ Curie temperature (T_C) in the FC state is ~ 20 K higher (when $E = 2$ kV/cm) than
72 that in the ZFC state, and that the R phase of the ZFC state is replaced by M_C ^{6,20}. Several neutron
73 and x-ray diffraction studies have been performed to determine the origin of the high
74 piezoelectricity in PZN-xPT by gradually increasing E at fixed temperature, thereby providing a
75 link between the piezoelectric properties and the structural parameters^{5,20,21}. However, the
76 underlying mechanism(s) cannot be fully understood without first understanding the structural
77 evolution of the MPB in the FC state.

78 In this paper, we report the results of an x-ray diffraction (XRD) study performed with high
79 resolution on single crystal PZN-xPT compositions located near the MPB in both ZFC and FC
80 states. Our findings are summarized in Figure 1. The open and solid circles represent data
81 reported previously by Kuwata *et al.*²² and La-Orauttapong *et al.*⁶, respectively. The vertical
82 dotted lines and the shaded region represent the MPB in the ZFC state. The solid squares
83 represent the phase transition temperatures we measured using XRD in the FC state with $E = 1$
84 kV/cm $// [001]$ together with those previously reported by Ohwada *et al.*²⁰ (shaded circles). The
85 modified phase diagram demonstrates that the MPB is quite fragile, and can be either destroyed
86 or reconfigured/created by application of $E // [001]$. The phase diagram also shows that the
87 temperature range for the stability of the T phase is significantly extended by an applied electric
88 field E , and the phase transformation sequences and temperatures are discussed within that
89 context.

90

91

II. EXPERIMENTAL DETAILS

92 Single crystals of PZN-4.5%PT and PZN-6.5%PT (provided by Microfine Materials Tech,
93 Singapore) with dimensions of $2 \times 2 \times 4 \text{ mm}^3$ and $2 \times 0.2 \times 4 \text{ mm}^3$, respectively, were cut with
94 $\{100\}$ faces, and all faces were polished to $0.25 \mu\text{m}$. Gold electrodes were deposited on the largest
95 top and bottom surfaces, which we designate as (001) faces. Additionally, ferroelectric (non-
96 relaxor) single crystals of PMN-55%PT and BaTiO_3 (Shanghai Institute of Ceramics) with
97 dimensions of $3 \times 3 \times 0.5 \text{ mm}^3$ were prepared with the large surface normal oriented along [001]
98 and polished to $0.25 \mu\text{m}$ for use in a contrast experiment. Diffraction measurements were then
99 performed with the scattering vector \mathbf{Q} oriented along [001]. Diffraction measurements were also
100 performed along [H00] and [HH0] on the PZN-4.5%PT crystals. For the PZN-6.5%PT crystals,
101 however, after finishing the measurements along [00L] the electrodes were removed using a
102 polishing blanket with $0.25 \mu\text{m}$ aluminum powder; new electrodes were then created by applying
103 silver paint to one pair of opposing faces perpendicular to the original (001) faces. Diffraction
104 measurements were then performed using a Philips MPD high-resolution system, which is shown
105 schematically in figure 2 (a). An incident monochromatic x-ray beam was produced by a line-
106 focus x-ray source together with a two-bounce hybrid monochromator using Ge (220) crystals.
107 The system was equipped with an open three-circle Eulerian cradle, which enabled samples to be
108 rotated (φ movement), tilted (ψ movement), and rocked (ω scans). A domed hot-stage was
109 mounted on the cradle, and the temperature was computer controlled. A Ge (220) cut crystal was
110 used as analyzer in which the diffracted beam undergoes three reflections within the groove
111 before entering the detector. The x-ray beam size was chosen to be $3 \times 3 \text{ mm}^2$, and the wavelength
112 was that of $\text{Cu K}_\alpha = 1.5406 \text{ \AA}$. The x-ray generator was operated at 45 kV and 40 mA. Under
113 these conditions, the instrumental wave vector resolution at (200) is 0.0068 degrees in 2θ full-
114 width at half-maximum (FWHM). The lattice parameters were obtained from radial (ω - 2θ) scans

115 measured across the (002), (200), and (220) Bragg peaks. All of these scans were performed
116 using an angular step size of 0.002° and an integration time of 2s. To determine the domain
117 configurations, reciprocal-space mesh scans (RMS) were measured around the (002) and (200)
118 or (020) Bragg peaks in the (H0L) or (0HL) zones, and around (220) in the (HHL) zone. These
119 were generated by performing a sequence of ω - 2θ scans at different ω offsets using a step size of
120 0.01° with an integration time of 0.5s (see figure 2 (b)) and are shown as intensity as a function
121 of reciprocal lattice position (in rlu). Each measurement cycle began by heating to 600 K to
122 anneal the crystals in order to decrease the internal strain²³; measurements were subsequently
123 taken on cooling. At 520 K, the cubic lattice constant for PZN-6.5%PT is $a = 4.054 \text{ \AA}$; the
124 corresponding cubic reciprocal lattice unit (or 1 rlu) is $a^* = 2\pi/a = 1.550 \text{ \AA}^{-1}$. All reciprocal-
125 space mesh scans shown here are plotted in reciprocal lattice units.

126 We note that the x-ray penetration depth ($1/e$) due to absorption in these PZN-xPT crystals at
127 (200) is only $\sim 2.6 \text{ \mu m}$ ²⁴, i.e, our diffraction measurements probe only the near-surface region.
128 Normally, this is more than sufficient to determine the bulk structure of most materials.
129 However, this is not the case for relaxors. An anomalous skin effect spanning the top most 50
130 \mu m to 100 \mu m of the crystal surface has been reported in single crystals of PZN-xPT, PMN-xPT,
131 and $\text{Na}_{1/2}\text{Bi}_{1/2}\text{TiO}_3$ (NBT) in which the near-surface crystal structure differs from that of the
132 bulk²⁵⁻²⁷. This is an extremely important point because the small x-ray penetration depth means
133 that the majority of the x-rays scatter from just the first one or two microns of the crystal surface,
134 and this will produce variability in the diffraction peak profiles and lattice parameters. We will
135 discuss this issue further in the following sections.

136 In order to investigate the surface domain configuration of PZN-xPT, Piezoresponse Force
137 Microscope (PFM) measurements were also performed using an Atomic Force Microscope

138 (AFM, Bruker multimode 8) with an open loop controller and a conductive AFM tip (MESP-RC,
139 Co/Cr coating, 35 nm tip radius) under contact mode. Temperature control between 300 K and
140 520 K was obtained using a Bruker Multimode heater stage with an accuracy of 0.5 °C.

141

142 III. PHASE TRANSITIONS, LATTICE PARAMETERS, AND PHASE

143

DIAGRAMS

144 Figure 1 displays the composition-temperature phase diagram for both ZFC and FC ($E =$
145 1kV/cm) conditions and summarizes the main results of this study. To obtain a more detailed
146 picture of how the phase transitions in PZN-xPT are affected by an electric field, x-ray
147 measurements were performed on cooling under electric fields of $E = 0, 1,$ and 2 kV/cm applied
148 parallel to [001]. The resulting electric field-temperature phase diagrams determined for PZN-
149 4.5%PT and PZN-6.5%PT are summarized in Figure 3. The transition temperatures were
150 determined by following the evolution of the lattice parameters and peak profiles. Details of the
151 XRD measurements and data analysis are given in the next sections.

152 A. Phase transitions and lattice parameters in ZFC PZN-xPT

153 The ZFC lattice parameters were measured by heating the crystal to 600 K, annealing for 30
154 minutes, and then performing radial scans through the pseudocubic (200) and (220) Bragg peaks
155 on cooling. Data from scans measured at five different temperatures are shown in Figure 4 for
156 PZN-4.5%PT. Two surprising features are immediately evident: (1) the Bragg peak profiles are
157 asymmetric in the cubic phase, particularly for (200); and (2) the Bragg peaks broaden markedly
158 on cooling into the purported T phase. The peak asymmetry is unexpected because it is absent in
159 radial scans measured using the identical x-ray set-up in the cubic phases of single crystal
160 specimens of BaTiO₃ and PMN-55%PT, neither of which is a relaxor (see Fig. 11). The

161 asymmetry is therefore a real effect and indicates the presence of a significant lattice gradient
162 (strain) within the near-surface region of the relaxor ferroelectric crystals. This finding is
163 consistent with the previous studies of the anomalous skin effect in PZN-xPT²³ and PMN-xPT²⁵
164 mentioned earlier. In particular, the neutron study by Conlon *et al.* on pure PMN found that the
165 lattice parameter varies as a function of depth measured from the crystal surface over a range of
166 order 100 μm ²⁸. The broadening of the Bragg peaks on cooling is equally unexpected because it
167 indicates that no long-range ordered (LRO) phase transitions take place in this material in the
168 ZFC state over this temperature range within the crystal volume probed by the x-ray beam. The
169 broadening Bragg peaks is discussed in Sec.IV.

170 For PZN-4.5%PT, evidence of a short-range-ordered *T*-like phase is apparent near 420 K by
171 the Gaussian fit in the left column of Fig. 4 at 400K. On further cooling, a continued coexistence
172 of *C* and *T*-like phases is observed until a transition into a new structure occurs near 380 K.
173 Interestingly, PZN-4.5%PT exhibits a *T*-like phase only in the presence of a coexisting *C* phase.
174 The *a*-domains of the *T*-like phase are not apparent along the (002) zone. The tetragonal *c*-
175 domain nucleation and growth in the *C*-phase has also been observed in a new generation of
176 relaxor ferroelectric single crystals²⁹, where the tetragonal *a*-domains were observed only on
177 further cooling. The *T*-like diffraction features are discussed in Sec. IV (see Fig.10). The *c*-axis
178 lattice parameter for the *T*-like phase is shown in Fig. 5, but the *a*-axis lattice parameter could not
179 be determined. Ohwada *et al.* performed neutron diffraction measurements on PZN-8%PT and
180 concluded that the ZFC structure at low temperature is not R^{20} , as had previously been accepted⁶.
181 Subsequent high-energy x-ray studies by Xu *et al.* on PZN²⁶, and high-resolution neutron studies
182 by Gehring *et al.*³⁰ on PMN-10%PT, also showed that the low temperature bulk phase is not *R*.

183 As the true ground state bulk crystal symmetry was unknown, the bulk phase was named phase
184 X^{19} , which designates a distorted structure within an average cubic phase²⁰.

185 According to the accepted zero-field PZN-xPT phase diagram^{6,22}, one expects a transition to
186 a LRO R phase for PZN-4.5%PT below ~ 400 K. Assuming a multi-domain sample, this should
187 manifest itself as a narrow single peak at (200) and two sharp peaks at (220). However, from
188 Fig.4 we see that at 385 K the pseudocubic (200) peak profile remains extremely broad and
189 continues to exhibit a weak, secondary peak on the low-angle side, both of which are
190 inconsistent with a LRO R phase. But on cooling to 350 K and then to 300 K the (200) peak
191 profile becomes increasingly better described by a single broad peak. At the same time, the
192 (220) peak profile gradually exhibits an increasingly stronger peak splitting, although it too
193 remains very broad. These data are thus consistent with the gradual formation of a SRO R phase
194 that is limited to the near-surface region in PZN-4.5%PT, which matches the conclusions Xu *et*
195 *al.*²⁴, who observed a SRO R phase in the near-surface region of PZN-4.5%PT using 10.2 keV x-
196 rays, but a less-distorted (smaller rhombohedral angle) R phase using 67 keV x-rays, which
197 penetrate much deeper into the crystal. The behavior in Fig. 4 is also reminiscent of the x-ray
198 diffraction study of single crystal PZN by Lebon *et al.*³¹ who observed that the $C \rightarrow R$ transition
199 occurs gradually between 385 K to 325 K and could be described by the formation of nanometer-
200 sized R domains that grow in number, but not in size, on cooling, thus leading to very broad x-
201 ray diffraction peak profiles.

202 We also performed radial scans at (002); these are shown in the bottom panel (300 K) on the
203 left-hand column in Fig. 4. It can be seen that the positions of the (200)_C and (002)_C Bragg peaks
204 do not coincide, whereas above 430 K they do. This is possibly due to there being a different
205 surface strain between (200) and (002), which correspond to different faces of the same crystal,

206 or to an undetermined symmetry at the surface layer of relaxors. The resulting lattice parameters
207 are given in Fig.5, which were determined by analyzing the (200) and (002) peak lineshapes. The
208 c -axis lattice parameter increases and the a -axis lattice parameter decreases on cooling,
209 analogous to the temperature evolution of the T lattice parameters. Further details regarding this
210 analysis are provided in Sec. IV. Similar results were obtained for PZN-6.5%PT (data not
211 shown), and the phase transition temperatures agreed well with those of the accepted ZFC phase
212 diagram^{6,22}.

213

214 **B. Phase transitions in [001] FC PZN-xPT**

215 We now discuss the effects of an electric field on the sequence of phase transitions in PZN-
216 xPT in the FC state. The crystals were initially annealed at 600 K after which fields of $E = 1$ and
217 2kV/cm were successively applied parallel to [001]. The phase transformational sequence in the
218 FC state was then studied on cooling by conducting radial and reciprocal-spacer mesh scans
219 performed close to the pseudocubic (002), (200), and (220) Bragg peaks.

220 For PZN-4.5%PT under $E=1\text{kV/cm}$, the phase transformational sequence is
221 $C \rightarrow T \rightarrow M_C \rightarrow M_A$, where the M_C phase coexists with the T phase over a narrow temperature
222 range. At $E = 2\text{kV/cm}$, the transformational sequence changes to $C \rightarrow T \rightarrow M_A$. The difference in
223 these two sequences indicates that the left side of the MPB in the FC state is located near $x=4.5$
224 for moderate E field. Figure 6 shows the evolution of the pseudocubic (200) Bragg peak profiles
225 with temperature for (a) $E = 1 \text{ kV/cm}$ and (b) 2kV/cm . At high temperatures, the system is cubic,
226 thus the (200) peak is not split; but the lattice parameter determined from (002) radial scans (data
227 not shown) is always slightly larger than that determined from (200) radial scans (see Fig.9 a).
228 On cooling, the crystal structure transforms to T near 440 K for $E=1\text{kV/cm}$ and 445 K for

229 $E=2\text{kV/cm}$. However no T -related splitting of either the (200) or (002) Bragg peaks was
230 observed ostensibly because the field-cooling process produced a predominantly single-domain
231 state. This is evident from the reciprocal-space mesh scans shown in [Figs.7 \(a-c\)](#). For this reason,
232 the c and a -axis lattice parameters were determined from radial scans performed at (002) and
233 (200), respectively. The thermal variation of the lattice parameters is shown in [Fig.9 \(a\)](#).

234 At 380 K and $E=1\text{kV/cm}$, the crystal adopts an M_C (b -domain) phase, which coexists with the
235 T phase. This conclusion is supported by the presence of two peaks in the mesh scan at (220)
236 shown in [Fig.7 \(f\)](#). A tendency of the transverse scan at (200) to split was also observed, even
237 though the contour maps shown in [Fig.7 \(d\)](#) and [\(e\)](#) around (002) and (200) appear to be single
238 peaks. This is presumed to be due to a small volume fraction of M_C . Interestingly, when the
239 sample is heated back up to 520 K and the electric field is increased to 2kV/cm , no evidence of
240 an M_C phase is observed in the mesh scan at (200) and (220) (data not shown). The observation
241 of an M_C (b -domain) phase under $E=1\text{kV/cm}$ implies that the left side of the MPB in the FC state
242 is located near $x=4.5$, as shown in [Fig. 1](#). The disappearance of the M_C b -domains when
243 $E=2\text{kV/cm}$ demonstrates that the MPB is fragile because it changes dramatically in the presence
244 of relatively weak applied electric fields. At the same time, the T phase becomes increasingly
245 stable with increasing $E//[001]$. **We note here** that the M_C phase component was indexed
246 following the phase transformational sequence of PZN-6.5%PT crystals, but that it was difficult
247 to determine in PZN-4.5%PT.

248 On further cooling, an M_A phase appears near 375 K for both $E=1\text{ kV/cm}$ and 2kV/cm , as
249 shown in [Fig.6](#). The appearance of the M_A phase is evident in the reciprocal-space mesh scans
250 (see [Figs.7 g-i](#)). The contour maps exhibited a single peak around the (002) zone, revealing that
251 the c axis is fixed along the direction that E is applied. The (200) peak exhibits a splitting along

252 the transverse direction, i.e., $(220) - (\bar{2}20)$ twin peaks. These are the signatures of the M_A
253 domain configuration. However, the contour map around (220) does not reveal the signature
254 triplet splitting of the M_A phase (i.e., one b -domain, containing two a -domains)^{19,32}, as shown in
255 Fig.7 (i), instead one b -domain and a single a -domain were apparent. This difference might be
256 related to defects in the crystals.

257 For PZN-6.5%PT, a phase transition sequence of $C \rightarrow T \rightarrow M_C \rightarrow M_A$ is found in the FC state,
258 similar to that for $x=4.5$. However, in this case the M_C phase is stable over a wider temperature
259 range. For $E=1\text{kV/cm}$, the $(002)_C$ peak disappears with decreasing temperature near 440 K and a
260 $(200)_T$ peak develops, demonstrating a $C \rightarrow T$ transformation. Reciprocal-space mesh scans reveal
261 a single domain configuration for the T phase (see Figs.8 a-c). On cooling to 350 K, a $T \rightarrow M_C$
262 phase transition is found (see Figs. 8 d-f). The pseudocubic (220) peak splits into two peaks
263 along the transverse direction; whereas, the (002) remains a single peak. Interestingly, a single
264 domain is observed around (200) and (020) , which is discussed in detail in section IV. The M_C
265 symmetry is also evident in the temperature evolution of the lattice parameters (see Fig.9 b). The
266 b -axis lattice parameter in the M_C phase decreases continuously with temperature following the
267 a -axis parameter in the T phase³². In the ZFC state, it is worth noting that the MPB lies over a
268 narrow compositional range of $9\% < x < 11\%$. However, in the FC state, the M_C phase was clearly
269 present near $x=6.5$ over a wide temperature range. This difference demonstrates that the
270 application of an electric field along $[001]$ bends the MPB over towards the low PT side of the
271 phase diagram.

272 A third transition to an M_A phase is observed on cooling to 310 K. As shown in Figs.8 (g-i),
273 the pseudocubic (200) peak splits into two peaks along the transverse direction (i.e., $(220) -$
274 $(\bar{2}20)$ twin peaks), the (220) peak splits into three peaks (i.e., one b -domain (020) peak and two

275 a -domains (200) – ($\bar{2}$ 00) peaks), and the (002) peak remains a single peak with the c -axis fixed
276 by the direction along which E is applied. This domain configuration is well described by the M_A
277 cell in which a_m and b_m lie along the tetragonal $[\bar{1}\bar{1}0]$ and $[1\bar{1}0]$ directions, and c_m is close to the
278 $[001]$ axis¹⁶.

279

280 C. Lattice parameters for [001] FC PZN-xPT

281 To clarify the effects of an electric field on the phase transition sequence in PZN-xPT, the
282 temperature dependences of the lattice parameters for both PZN-4.5%PT and PZN-6.5%PT
283 crystals in the FC state for $E=1\text{kV/cm}$ are shown in Fig.9. The cubic lattice parameters for both
284 compositions were determined from radial scans measured at (002) and (200). It can be seen that
285 the values agree well with each other. The tetragonal lattice parameters (a_T , c_T) were extracted
286 from the (200)_T and (002)_T peaks, respectively and cross-checked with scans measured at (220)_T.
287 As expected, the tetragonality ($c/a-1$) becomes more pronounced with decreasing temperature.

288 Because only one of the b -domains in the M_C phase is observed for PZN-4.5%PT, not all of
289 the lattice parameters could be determined (see Fig.9 a). For PZN-6.5%PT the (002)_T peak
290 abruptly shifts to higher 2θ values at 350 K, indicating that the c -axis contracts at the $T \rightarrow M_C$
291 transition, whereas the (200)_T peak remains a single peak, corresponding to the b -domain
292 (020)_{MC}, and shifts continuously to higher 2θ values with decreasing temperature (see Fig.9 b).
293 The (220)_T peak splits into two peaks along the transverse direction: (220) – ($\bar{2}$ 20) twin peaks,
294 from which the values of a_m and the monoclinic angle β_C can be extracted.

295 On cooling to 300 K, both PZN-4.5%PT and PZN-6.5%PT transform into the M_A phase. The
296 c -axis lattice parameter in the M_A phase was calculated from the pseudocubic (002) radial scans
297 and the monoclinic angle β_A . The lattice parameters a_M and b_M were extracted from (220) radial

308 scans. For PZN-4.5%PT, the b -axis lattice parameter of the M_A phase exhibits a discontinuous
309 change at the transition, which was unlike that for PMN-xPT, where $b_M/\sqrt{2}$ and a_T continuously
300 decrease with decreasing temperature³³.

301

302

IV. DISCUSSION

303

304 The study of the ground state and the diffraction peak profiles in relaxors in the ZFC state
305 using x-ray diffraction methods began with our attempts to study the phase transitions and MPB
306 in the FC state. During these measurements, we noted a significant asymmetry in the diffraction
307 profiles in the cubic phase near the Curie temperature in the ZFC state. As shown in Fig. 4, the
308 $(200)_C$ and $(002)_C$ Bragg peaks always exhibit an asymmetric **lineshape**, even at temperatures
309 well above the Curie temperature. This asymmetry is well-described by a very broad peak at low
310 2θ that coexists with a sharp peak **at higher 2θ** , and it increases on cooling towards the purported
311 $C \rightarrow T$ transition temperature. Both of these observations can be understood by the existence of a
312 near-surface region, or “skin,” of the crystal that has a depth-dependent lattice spacing, i.e. a
313 lattice gradient that spans at least several microns, which is consistent with the anomalous
314 relaxor skin effect³⁹. A comparison of the ZFC and [001] FC diagrams of PZN-xPT in Fig. 1
315 reveals several interesting findings: (i) that the initial R (or M) phase of the ZFC state is replaced
316 by an M_A phase in the FC state; (ii) that the initial O phase in the ZFC state is replaced by an M_C
317 phase in the FC state; (iii) that the MPB in the ZFC diagram, which is nearly vertical and located
318 near $8\% < x < 11\%$, is destroyed/created in the FC state by modest fields of $E=1$ kV/cm and
319 2kV/cm; and (iv) that the stability of the T phase is extended to lower PT compositions and
320 higher temperatures by the application of an electric field.

321

322 A. Asymmetric diffraction profiles and phase coexistence at high temperature

323 (i) Near the Curie temperature in the ZFC state

324 Figure 10 (a) shows the temperature dependence of the $(002)_C$ Bragg peak profile for ZFC
325 PZN-4.5%PT. One can see that the peak intensity decreases discontinuously and the peak width
326 broadens substantially near 420 K. Figure 10 (b) shows representative diffraction peak profiles at
327 500 K, 400 K, and 300 K. A fit of the $(002)_C$ Bragg peak at 500 K to a single Gaussian function
328 shows that the profile is not symmetric: it exhibits a weak shoulder on the low angle side, which
329 is consistent with the presence of a near-surface lattice gradient as reported by Conlon *et al*²⁸.
330 This asymmetry becomes far pronounced at 420 K. Therefore, below 420 K, the $(002)_C$ peak
331 profiles were fit using two Gaussian peaks to test the possibility that the low-angle shoulder
332 might be the result of a coexistence of a weak (low volume fraction) T -phase and a strong C -
333 phase. However, on cooling to 380 K, a broadened peak is obtained, which we fit to a single
334 Gaussian peak. The temperature dependence of the FWHM is given in Figure 10 (c). The large
335 FWHM indicates that the T phase is not LRO and instead consists of SRO regions. We speculate
336 that these SRO tetragonal regions coexist in a cubic matrix around the Curie temperature. After
337 cooling in an electric field $E = 1\text{kV/cm}$, a well-defined LRO T phase is observed and manifested
338 by the presence of tetragonal c -domains along $[001]$ and a -domains along $[100]$ (radial scans not
339 shown in Fig. 10, but the lattice parameters are given in Fig. 9). Furthermore, recently a distinct
340 tetragonal diffraction profile in the FC state with $E//[001]$ was observed in a single crystal of the
341 related relaxor ferroelectric system $\text{Pb}(\text{In}_{1/2}\text{Nb}_{1/2})\text{O}_3\text{-Pb}(\text{Mg}_{1/3}\text{Nb}_{2/3})\text{O}_3\text{-PbTiO}_3$ (PIN-PMN-
342 PT)²⁹. Short-range-ordered tetragonal regions may cluster together and grow into a conventional
343 long-range order phase under application of an E -field²⁹.

344 Relaxor ferroelectric single crystals of PMN-xPT and PZN-xPT are known to possess a
345 surface layer $\sim 100 \mu\text{m}$ thick that is structurally distinct from the bulk, a phenomenon known as
346 the anomalous skin effect^{34,35}. The internal strains in these materials, which persist even after
347 annealing at high temperature, will result in a d -spacing gradient, that could produce a broadened
348 and asymmetric x-ray diffraction profile^{26,34,36}. Given that the absorption-limiting penetration
349 depth ($1/e$) of Cu $K\alpha$ x-rays is about 2-3 μm in PZN-xPT^{13,37}, the most likely explanation for the
350 asymmetric diffraction peak profiles in the cubic phase and the broad, T -like diffraction feature
351 in the cubic matrix is the skin effect, as the low-energy x-rays used here will scatter
352 predominantly from the first one to two microns of the crystal surface. **Even in the non-relaxor**
353 **materials SrTiO_3 and LaAlO_3 , a related skin effect has been reported, and a distinct symmetry**
354 **observed between the surface near region and the bulk^{38,39}**. Neutrons, by contrast, being charge-
355 neutral particles, are able to penetrate far more deeply than x-rays into crystals; they therefore
356 provide structural information related to the average bulk crystal symmetry. Prior neutron studies
357 have revealed symmetric peak profiles in the bulk of relaxor PZN-xPT crystals⁴⁰. Hence the
358 difference between neutron and x-ray diffraction profiles **highlighted** in this study provides
359 evidence that the asymmetric peaks likely result from this skin effect. Furthermore, Ohwada *et*
360 *al.* studied the c -axis lattice variation using both neutron and x-ray techniques during the R - M_A -
361 M_C phase transition sequence, and they found a sharp jump in the c -axis lattice spacing using x-
362 rays that was not reproduced by neutron methods³⁶. The difference between the diffraction
363 features in the near-surface and bulk regions of the crystal **suggest the presence of** a non-uniform
364 strain distribution within the skin. In the present study, even under an applied electric field E , we
365 observe a notably asymmetric diffraction profile in both the high and room temperature phases,

366 as shown in Fig.6, which differs from the findings obtained from neutron diffraction. This is also
367 consistent with the idea that the asymmetric diffraction profile is due to the skin effect.

368 In order to further elucidate the skin effect, additional diffraction measurements were made
369 of (200)_c Bragg peaks in single crystals of the conventional non-relaxor ferroelectrics BaTiO₃
370 and PMN-55%PT in the cubic phase, as the asymmetric peak broadening is a measure of the
371 strain distribution in the surface layer of relaxors^{13,23,36}. The intensity of each diffraction peak is
372 normalized to a value of 100 and plotted on a linear scale, as shown in Fig. 11. From these data it
373 can be seen that the size and strength of the diffraction peak asymmetry in the relaxors is much
374 larger than that in non-relaxor ferroelectric crystals. These findings demonstrate that the relaxor
375 PZN-4.5%PT and PZN-6.5%PT crystals possess a significant skin effect.

376 Piezo-force microscopy (PFM) is an intrinsically surface-sensitive technique, and so it cannot
377 access the interior/bulk domain structure of relaxor crystals. Figure 12 (a) shows an AFM image
378 illustrating the surface roughness (10 μm ×10 μm) for a PZN-4.5% crystal. Vertical PFM phase
379 images were then acquired at 400 K, 430 K, and 450 K on heating, as shown in Figs. 12 (b-d). It
380 is interesting to note that ferroelectric domain structural features, which weaken with increasing
381 temperature, are seen that persist to several tens of degrees above the bulk Curie temperature.
382 We note that similar observations have previously been reported for PZN-12%PT³⁵. Again, these
383 features can be attributed to strain gradient distributions, unique atomic configurations, and/or a
384 distinct stoichiometry of the surface layer^{34,35,41}.

385 Diffuse scattering such as Huang scattering, could also give rise to an for asymmetric
386 diffraction profile⁴². However, we argue that diffuse scattering cannot be the cause of the
387 asymmetric diffraction peak profiles observed in our study. In PZN-xPT, the diffuse scattering
388 intensity is orders of magnitude weaker than the Bragg peak intensity, whereas in this study the

389 asymmetry is visible even when the intensity is plotted on a linear scale (see Fig.11). In addition,
390 the reciprocal-space mesh scans (see Figs.7-8, also plotted on linear scale) show no evidence of
391 the well-known butterfly-shaped intensity contours around (200) or the elliptically-shaped
392 contours around (220)^{43,44}. For these reasons, we believe that skin effect is the most possible
393 cause of the **diffraction peak asymmetry in the cubic phase**. The skin effect would also explain
394 why the diffraction peaks broaden below the Curie temperature: Xu *et al.* showed that the size of
395 the structural distortion decreases with increasing distance from the crystal surface in PZN-xPT²⁴
396 and PZN⁴⁵, thus the very-near surface region of the crystal never achieves long-range order.

397

398 **(ii) Near the $C \rightarrow T$ phase transition region in the FC state**

399 **Broadened diffraction peaks are** also notable in the vicinity of the $C \rightarrow T$ transition
400 temperature, **and are seen in transverse scans of the** (200)_T and (220)_T Bragg peaks in PZN-
401 6.5%PT, whereas that for (002)_T exhibits a sharp peak profile, as shown in Fig.8 (a-c). Similar
402 profiles have also been observed in ternary PIN-PMN-PT relaxor crystals. In order to determine
403 the underlying mechanism for this phenomenon, rocking curves (ω scans at fixed 2θ values)
404 were performed around (002)_T, (200)_T and (220)_T, as shown in Fig.13, where **one or more**
405 **Gaussian functions were fit to each curve**. The results show a single peak around (002)_T and
406 doublets around (200)_T and (220)_T. The splitting along the *transverse direction* are similar to
407 those found in the M_C phase under application of **an electric field $E//[001]$** ³². However, the
408 crystals are unambiguously in the T -phase region, as can be seen from radial scans and the
409 evolution of the lattice parameters with temperature (see Fig.9 (b)). The splitting of the rocking
410 curves around the (200) and (220) peaks in the tetragonal region may be interpreted as evidence
411 that the M_C phase is a “ferroelectric adaptive phase”⁴⁶⁻⁴⁹. Under application of moderate E along

412 [001], the polarization vectors of the tetragonal regions will tend to align with the E field,
 413 however, a fraction of the vectors may remain perpendicular: thus, the domain state is referred to
 414 as a pseudo-mono domain configuration. Such polydomain ferroelastic crystals consist of
 415 structural twins that accommodate elastic strain^{47,50}. Wang has predicted that the twinned a - and
 416 c -domains in the T -phase can produce a superlattice of M_C symmetry if they are adaptive^{48,49}. In
 417 turn, this leads to a splitting in the ω scans along the $(200)_T$ and $(220)_T$ peaks, given as

$$418 \quad \beta_C = 90^\circ + 2Av(1-\nu)\left(\tan^{-1} \frac{c_t}{a_t} - 45^\circ\right); \quad (1)$$

419 where β_C is the angle of the low symmetry M_C phase, A is a fitting constant (close to 1), and ν is
 420 the volume fraction of the twinned a - or c -domains. The diffraction broadening feature along the
 421 transverse direction in Fig.8 may result from twin-related tetragonal nano-variants, not being
 422 perfectly stable with respect to each other in a manner that achieves complete stress
 423 accommodation. We note that this feature (i.e., diffraction broadening along the transverse
 424 direction) is more profound in a poled PIN-PMN-PT crystal¹², indicating poled relaxor crystals
 425 are dominated by nanotwins. These results also provide indirect evidence that the nanotwin
 426 boundary is the origin of high piezoelectric properties for relaxor ferroelectric crystals⁵⁰.

427

428 **B. Crystal structure at 300 K**

429 As shown in Fig. 4, the $(002)_C$ and $(200)_C$ Bragg peaks at 300 K are significantly different,
 430 much more so than in the high temperature region. As a result, the difference between the a - and
 431 c -axis lattice parameters determined from the $(200)_C$ and $(002)_C$ peaks is notably larger than the
 432 experimental errors (see Fig. 5). These findings show that the ground state for PZN-4.5%PT is
 433 not a long-range ordered R -phase (nor is that for PZN-6.5%PT, data not shown). This is
 434 inconsistent with previous observations by single crystal and powder diffraction, via low and

435 high energy x-ray beams^{6,25}. Our findings are similar to those for PZN-8%PT reported by
436 Ohwada *et al.*, where an unknown ground state designated as “phase X” was conjectured. Also
437 puzzling was the difference between the peak intensities at $(200)_C$ and $(002)_C$ and whether **or not**
438 this difference was intrinsic. The d -spacings were determined by the positions of the diffraction
439 peaks, which can be influenced by the surface condition (i.e., $(200)_C$ and $(002)_C$): such as
440 mechanically-induced stain, defect or stoichiometric inhomogeneity²³. However, before each
441 measurement, the crystals were annealed above 600 K for 30 mins to relax the residual surface
442 strain. Interestingly, the intensity and FWHM of the $(002)_C$ and $(200)_C$ peaks exhibited
443 differences above the Curie temperature (see Fig.4 at 430 K), the difference increased with
444 decreasing temperature (i.e. as the c -lattice increased, and the a -lattice decreased).

445 In addition to the difference between the diffraction intensities at $(002)_C$ and $(200)_C$, the peak
446 profiles were highly asymmetric, as can be seen from the one-peak Gaussian mode fits shown in
447 Fig. 10 (b). This asymmetry indicates that additional peaks may exist within the broad one, but
448 were hard to distinguish. We note that the asymmetry of the $(200)_C$ peak is consistent in peak
449 position ranges with the $(002)_C$ (see Fig.4). We thus could speculate that the ground state might
450 be a monoclinic phase, rather than the distorted cubic “phase X” as proposed by Ohwada *et al.*

451 The FWHM of the $(200)_C$ diffraction peak is much larger than expected given the resolution
452 of the Ge (220) cut crystal analyzer (see Fig. 10 c). The large FWHM most likely results from a
453 collection of micro-crystal boundaries contributing to the total scattering intensity²⁶. An
454 explanation for this broadening nature has conventionally been a skin effect, which is known to
455 effect x-ray studies of relaxor crystals due to the limited x-ray penetration depth²⁶. The neutron
456 study of both powder and single crystal samples of PMN-xPT by Phelan *et al.*¹³ has shown that
457 the skin effect vanishes on the tetragonal side of the MPB, i.e. for Ti concentrations $x \sim 0.40$ and

458 higher. They presented a revised PMN-xPT phase diagram where the ground state was
459 designated as “short-range R/M ”¹³. Analogously, the ground state of PZN-xPT on the left side of
460 the MPB was indexed as a SRO monoclinic structure because they share similarly broadened
461 features. During a manuscript revision, Zhang et al.¹⁰ found experimental evidence that a LRO R
462 phase coexists with both LRO and SRO monoclinic regions on the Zr-rich side of the MPB of
463 PZT. These findings indicate the ground state of these relaxor solid solutions may be more
464 complex than previously thought.

465

466 **C. Extension of the T phase region by E**

467 It was found that the stability of the T phase is significantly enhanced by the application of an
468 electric field E for single crystals of PZN-xPT with $x=4.5\%$ and 6.5% , compositions that lie on
469 the left side of the MPB. Even though PZN-xPT crystals with $x>9\%$ (i.e., located on the right
470 side of the MPB) were not studied, one can make inferences from the related ternary PIN-PMN-
471 PT relaxor solid crystals, located near the MPB but to the right side. In this case, an E -field
472 induced enhancement of the T phase stability was clearly observed. We thus believe that this
473 phenomenon is a common feature for all relaxor crystals, and not strongly dependent on
474 compositions.

475

476 **(i) Extension of the T phase to higher temperatures**

477 In order to understand the extension of the T phase to higher temperatures (T) by the
478 application of an electric field E , a simple form of the classical Landau theory was employed.
479 Generally, the free energy (G) of the system, being a function of the mole fraction PT (x) and T ,

480 can be described as a symmetry-adapted Landau series with respect to the absolute value of the
 481 spontaneous polarization P in the unconstrained state,

$$482 \quad G(x, T, P) = \frac{1}{2} \alpha(x)(T - T_0)P^2 + \frac{1}{4} \beta(x)P^4 + \frac{1}{6} \gamma(x)P^6 - EP; \quad (2)$$

483 where $\alpha(x)$, $\beta(x)$ and $\gamma(x)$ are the coefficients of the various ordered terms, respectively. E is the
 484 normalized externally applied electric field, where it is also assumed that the polarization and E
 485 are parallel.

486 Our idea is to determine, in the simplest possible case, the E -field induced extension of the T
 487 phase. For a first-order phase transition, one can assume that $\alpha(x) > 0$, $\beta(x) < 0$, and $\gamma(x) > 0$. When
 488 $E=0$, $G(P)$ has two minima at $P \neq 0$ in addition to one at $P = 0$. For $T < T_C$, $G < 0$, so that a
 489 discontinuous transition occurs from $P=0$ into the state with two minima at $P \neq 0$. The
 490 paraelectric \rightarrow ferroelectric transition temperature T_C under $E=0$ can then be found as

$$491 \quad T_C = T_0 + \frac{3}{16} \frac{\beta(x)^2}{\alpha(x)\gamma(x)}. \quad (3)$$

492 From the Clausius-Clapeyron equation ($T_C(E) = T_C - \frac{\Delta P}{\Delta S} E$), where ΔP and ΔS are the
 493 discontinuous change in polarization and entropy at T_C), the Curie temperature T_C at various E is

$$494 \quad T_C(E) = T_C + \frac{4}{\alpha(x)} \sqrt{\frac{-\gamma(x)}{3\beta(x)}} E. \quad (4)$$

495 From Eq. (4), it is obvious that T_C increases with increasing E field when $\alpha(x) > 0$. This
 496 prediction that the T phase is extended by E applied parallel to $[001]$ is a common characteristic
 497 of all $T \rightarrow C$ transition that are 1st order, independent of the composition and the category of the
 498 crystals.

499

500 **(ii) Extension of the T phase to lower x**

501 As shown in Fig. 4, the coexistence of T and C phases was only found for PZN-4.5%PT
502 crystals in the ZFC state, where a $C \rightarrow$ SRO monoclinic transformation occurred on cooling.
503 However, for [001] PZN-4.5%PT crystals in the FC state, the T -phase existed independently of C
504 (see Fig. 6). This demonstrates that the T -phase can be extended to lower PT contents under E .

505 In the PZN- x PT solution, substitution of the $[\text{TiO}_4]^{4-}$ octahedron for the more complex
506 $[\text{Zn}_{1/2}\text{Nb}_{2/3}\text{O}_4]^{4-}$, results in an MPB separating R and T ferroelectric phases. The c/a ratio of the
507 T -phase weakens with decreasing x on approaching the MPB. PZN-4.5%PT can be considered as
508 a special composition in the diagram, where a gradual transition between T microdomains in a C
509 matrix and a macroscopic T phase begins to occur. If the T microdomains are much smaller than
510 the coherence length of x-rays, the average structure appears monoclinic or X by diffraction in
511 the ZFC state. However, in the FC state, the T microdomains align parallel to E , and thus a
512 macroscopic T phase is observed to sandwich the C and M_A ones on cooling.

513

514 **D. Destruction of old and creation of new MPB by E**

515 The most significant feature in Figure 1 is the destruction of the R/M and T MPB of the ZFC
516 state by a moderate E and creation of a new one. PZN-4.5%PT and PZN-6.5%PT undergo a
517 transformational sequence $C \rightarrow T \rightarrow M_C \rightarrow M_A$. This sequence is similar to that previously reported
518 for PZN-8PT by Ohwada *et al.*, except the present results reveal that the $M_C \rightarrow M_A$ transition is
519 decreased to room temperature by E .

520 In the ZFC state, the transformational sequence is $C \rightarrow T \rightarrow R$ or M for $x < 8\%$, while the
521 transformational sequence is $C \rightarrow T$ for $x > 11\%$. In the ZFC state, a MPB exists for $8\% < x < 11\%$,
522 which is nearly vertical separating R or M and T phases. However, under $E // [001]$, a structurally
523 bridging M_C phase is found near the MPB; and in particular, the vertical nature of the MPB was

524 transformed in the x - T field to being notably bent towards the lower x side. This M_C phase
525 appeared not only in the range of the MPB of the ZFC state of $8\% < x < 11\%$, but also over an
526 extended range of $4.5\% < x < 8\%$. To understand the tilting of the MPB, it is worth referring to the
527 polarization rotation path of PZN- x PT for $E//[001]$ as the polarization rotation path depends on
528 x . The bifurcated path indicates that the lowest free energy path for the various compositions is
529 different. Analogously, we conjecture that the lowest free energy path is also different in the
530 cooling process without (i.e., ZFC state) and with (i.e., FC state) an E field applied to a constant
531 composition, and for different compositions in the FC state. For PZN-6.5%PT, the polarization
532 rotation path is along $T \rightarrow R$ in the ZFC state, while in the FC state, the polarization first rotates
533 along the $T \rightarrow O$ path, and then abruptly jumps to $T \rightarrow R$ one. This results in a modified phase
534 transition sequence of $T \rightarrow M_C \rightarrow M_A$. Whereas, for low PT crystals (i.e., $x < 4.5\%$), the
535 polarization rotation path is along $T \rightarrow R$ in both ZFC and FC (e.g. moderate amplitude of
536 $E=1\text{kV/cm}$) states.

537

538 **E. Atypical M_C Domain configurations in FC PZN-6.5%PT**

539 Monoclinic symmetry allows for 24 possible domain states and thus normally results in very
540 complicated domain configurations. However, in PMN-PT and PZN-PT crystals, an applied
541 $E//[001]$ fixes the c axis, simplifying the configuration. The resultant signature polar vector
542 orientation and domain configuration for the M_C phase are schematically illustrated in Fig.14 (a).
543 In the HOL plane, there are only two b domains that are related by a 90° rotation about the c axis,
544 where each of these has two related a domains having an angle of β or $180-\beta$ with c_m . The
545 polarization vectors of each of these four domains is rotated under E in the monoclinic plane,
546 forming identical angles along the $[001]$.

547 An atypical domain configuration was observed in this experiment as shown in Fig.8 and
548 schematically illustrated in Fig.14 (b). As expected, a single peak was observed around the (002)
549 zone, illustrating that the c axis is fixed along the direction that E was applied. However, about
550 the (020) zone, only a single b domain was found that was slightly tilted along the longitudinal
551 direction, rather than containing two a domains in a typical case. Generally, in the M_C phase, the
552 a and b domains can be switched between each other about the c axis, as designated by shaded
553 and unshaded axis labels in Fig.14 (a). In turn, four polar vectors in the $a_m c_m$ plane are possible.
554 However, surface residual stress in the ferroelectric crystals can break this domain equivalence,
555 resulting in some domains being absent compared to the equilibrium configuration.

556

557

V. CONCLUSIONS

558 A comprehensive x-ray diffraction study of single crystal PZN-4.5%PT and PZN-6.5%PT
559 was performed on cooling under $E=0$ kV/cm, 1 kV/cm and 2kV/cm. In the ZFC state, the ground
560 state crystal structure of PZN-4.5%PT resembles a short-range-ordered monoclinic phase or a
561 distorted rhombohedral one due to the skin effect, which is consistent with a previous
562 synchrotron study by Xu *et al.* on the same compound²⁴. It was established that the phase
563 transformational sequence with decreasing temperature for both PZN-4.5%PT and PZN-6.5%PT
564 is $C \rightarrow T \rightarrow M_C \rightarrow M_A$ in the FC state. An [001] FC phase diagram was constructed based on these
565 diffraction data, and it was found that the phase stability and MPB were fragile to application of
566 moderate electric fields. The T phase region was found to be significantly extended by E . In
567 particular, the vertical nature of the MPB in the ZFC diagram was lost.

568

569

ACKNOWLEDGMENTS

570
571 The work at Nanjing University of Science and Technology was supported by the National
572 Natural Science Foundation of China (51602156 and 11134004), the Natural Science Foundation
573 of Jiangsu Province, China (BK20160824), the Fundamental Research Funds for the Central
574 Universities (30916011208 and 30916011104), and the Opening Project of Key Laboratory of
575 Inorganic function material and device, Chinese Academy of Sciences (KLIFMD-2015-01). The
576 US part of this collaborative work was sponsored by the Office of Naval Research (N00014-13-
577 1-0049) F. Xu is thankful for the support from the Jiangsu Natural Science Foundation for
578 Distinguished Young Scholars (BK20140035). Y.J. Wang thanks the discussion from Dr. Z.G.
579 Wang and C.T. Luo.

Figure captions

580
581
582
583 **Figure 1** PZN-xPT phase diagram near the MPB. Open circles represent the data for ZFC PZN-
584 xPT reported by Kuwata *et al.*²². Solid circles represent the more recent data for ZFC PZN-xPT
585 reported by La-Orauttapong *et al.*⁶ The symbols *R* (or *X*) and *O* designate the rhombohedral (or
586 *X*) and orthorhombic ZFC phases. Our data on FC PZN-4.5%PT and PZN-6.5%PT are plotted as
587 solid squares and included with those of Ohwada *et al.* for FC PZN-8PT (shaded circles). The
588 black dotted lines represent the MPB in the ZFC state, while the red dashed lines represent the
589 MPB in the FC state ($E = 1$ kV/cm // [001]). Our ZFC results are not shown in this figure (see
590 text), as they agree well with the ZFC results of La-Orauttapong *et al.*⁷.

591

592 **Figure 2** Schematic diagram of (a) Phillips MPD high resolution x-ray diffractometer and (b)
593 single and reciprocal-space mesh scans in the (HOL) zone. The rocking curve (ω scan) describes
594 a circular arc centered on the origin; the detector scan (2θ scan) follows the circumference of the
595 Ewald sphere; and the ω - 2θ radial scan describes a straight line pointing radially from the origin.
596 A typical reciprocal-space mesh scan centered on $(301)_C$ is shown.

597

598

599 **Figure 3** Electric field-temperature phase diagram for (a) PZN-4.5%PT and (b) PZN-6.5%PT in
600 the FC state with $E//[001]$. Arrows indicate the sequence of phase transitions on cooling. Solid
601 circles represent the respective transition temperatures as defined in the text. Lines are guides to
602 the eyes.

603

604 **Figure 4** Evolution of the pseudocubic $(200)_C$ and $(220)_C$ Bragg peak lineshapes **on cooling** from
605 the cubic phase to the short-range ordered monoclinic phase for PZN-4.5%PT. Open and solid
606 circles represent the $(200)_C$ and $(002)_C$ peak profiles in the C and short-range-ordered monoclinic
607 phases, respectively. **The square root of the diffracted x-ray intensity** is plotted in order to make
608 weak peaks and shoulders more visible.

609

610 **Figure 5** Lattice parameters of ZFC PZN-4.5%PT as a function of temperature.

611

612 **Figure 6** Evolution of the pseudocubic (200) Bragg peaks for PZN-4.5%PT cooled under (a) $E =$
613 1 kV/cm and (b) $E = 2 \text{ kV/cm}$, respectively, where $E // [001]$. **The square root of the diffracted x-**
614 **ray intensity is plotted in order to make weak peaks and shoulders more visible.**

615

616

617 **Figure 7** Reciprocal-space mesh scans centered on the pseudocubic (002), (200) and (220) Bragg
618 peaks at different temperatures for FC PZN-4.5%PT ($E = 1$ kV/cm // [001]).

619

620 **Figure 8** Reciprocal-space mesh scans centered on the pseudocubic (002), (200) and (220) Bragg
621 peaks at different temperature for FC PZN-6.5%PT ($E = 1$ kV/cm // [001]).

622

623 **Figure 9** Lattice parameters of FC (a) PZN-4.5%PT and (b) PZN-6.5%PT as a function of
624 temperature ($E = 1$ kV/cm // [001]). Dashed lines represent the respective transition temperatures
625 as defined in the text. The experimental uncertainty of the lattice parameters extracted from
626 $(002)_C$ and $(200)_C$ is less than 0.001\AA .

627

628 **Figure 10** (a) x-ray intensity contour map of the PZN-4.5%PT $(002)_C$ Bragg peak showing the
629 evolution of the width with temperature. (b) Representative $(002)_C$ Bragg peaks at 520 K, 400 K,
630 and 300 K. The data were fit using single-peak and two-peak Gaussian functions, respectively.
631 (c) Temperature dependence of the $(002)_C$ Bragg peak FWHM derived from the Gaussian fits.

632

633 **Figure 11** Profile of pseudocubic $(200)_C$ Bragg peak in the cubic phase for relaxor and normal
634 ferroelectric single crystals: (a) PZN-4.5%PT at 430K, (b) PZN-6.5%PT at 430K, (c) BaTiO₃ at
635 430K and PMN-55%PT at 570K, respectively. The intensity of each diffraction peak was
636 normalized in order to clearly reveal the asymmetrical and broadening features.

637

638 **Figure 12** (a) Topography AFM image of the surface roughness of PZN-4.5%PT single crystals
639 of an area of $10 \times 10 \mu\text{m}$ and (b) the corresponding phase image of PFM of the same region at
640 various temperatures. The surface ferroelectric domain configuration remains identical above the
641 bulk phase transition.

642

643 **Figure 13** (a) Comparison of rocking curves for FC PZN-6.5%PT in the tetragonal phase.

644

645 **Figure 14** Polar vectors and domain configurations in cubic Cartesian coordinates for the (a)
646 signature M_C phase and (b) atypical M_C phase observed in this work. The polar vector in the
647 monoclinic M_C phase lies in the $a_m c_m$ monoclinic plane, as designated by the arrows.

648

649 **References**

- 650 ¹ H. X. Fu and R. E. Cohen, *Nature* **403**, 281 (2000).
- 651 ² S. E. Park and T. R. Shroud, *Journal of Applied Physics* **82**, 1804 (1997).
- 652 ³ Y. Wang, J. Li, and D. Viehland, *Materials Today* **17**, 269 (2014).
- 653 ⁴ D. S. Paik, S. E. Park, S. Wada, S. F. Liu, and T. R. Shroud, *Journal of Applied Physics* **85**,
654 1080 (1999).
- 655 ⁵ B. Noheda, D. E. Cox, G. Shirane, J. Gao, and Z. G. Ye, *Physical Review B* **66**, 054104
656 (2002).
- 657 ⁶ D. La-Orautpong, B. Noheda, Z. G. Ye, P. M. Gehring, J. Toulouse, D. E. Cox, and G.
658 Shirane, *Physical Review B* **65**, 144101 (2002).
- 659 ⁷ D. Phelan, X. Long, Y. Xie, Z. G. Ye, A. M. Glazer, H. Yokota, P. A. Thomas, and P. M.
660 Gehring, *Physical Review Letters* **105**, 207601 (2010).

661 ⁸ D. E. Cox, B. Noheda, G. Shirane, Y. Uesu, K. Fujishiro, and Y. Yamada, *Applied Physics*
662 *Letters* **79**, 400 (2001).

663 ⁹ B. Noheda and D. E. Cox, *Phase Transitions* **79**, 5 (2006).

664 ¹⁰ N. Zhang, H. Yokota, A. M. Glazer, Z. Ren, D. A. Keen, D. S. Keeble, P. A. Thomas, and Z.
665 G. Ye, *Nature Communications* **5**, 5231 (2014).

666 ¹¹ B. Noheda, D. E. Cox, G. Shirane, R. Guo, B. Jones, and L. E. Cross, *Physical Review B* **63**,
667 014103 (2001).

668 ¹² Y. Wang, Z. Wang, W. Ge, C. Luo, J. Li, D. Viehland, J. Chen, and H. Luo, *Physical*
669 *Review B* **90**, 134104 (2014).

670 ¹³ D. Phelan, E. E. Rodriguez, J. Gao, Y. Bing, Z. G. Ye, Q. Huang, J. Wen, G. Xu, C. Stock,
671 M. Matsuura, and P. M. Gehring, *Phase Transitions* **88**, 283 (2015).

672 ¹⁴ B. Jaffe, *Piezoelectric Ceramics* (Academic Press, India, 1971).

673 ¹⁵ Y. Uesu, M. Matsuda, Y. Yamada, K. Fujishiro, D. E. Cox, B. Noheda, and G. Shirane,
674 *Journal of the Physical Society of Japan* **71**, 960 (2002).

675 ¹⁶ B. Noheda, D. E. Cox, G. Shirane, J. A. Gonzalo, L. E. Cross, and S. E. Park, *Applied*
676 *Physics Letters* **74**, 2059 (1999).

677 ¹⁷ A. A. Bokov and Z. G. Ye, *Applied Physics Letters* **92**, 082901 (2008).

678 ¹⁸ C. Ma, H. Guo, S. P. Beckman, and X. Tan, *Physical Review Letters* **109**, 107602 (2012).

679 ¹⁹ H. Cao, J. F. Li, D. Viehland, and G. Y. Xu, *Physical Review B* **73**, 184110 (2006).

680 ²⁰ K. Ohwada, K. Hirota, P. W. Rehrig, Y. Fujii, and G. Shirane, *Physical Review B* **67**,
681 094111 (2003).

682 ²¹ B. Noheda, Z. Zhong, D. E. Cox, G. Shirane, S. E. Park, and P. Rehrig, *Physical Review B*
683 **65**, 224101 (2002).

684 ²² J. Kuwata, K. Uchino, and S. Nomura, *Ferroelectrics* **37**, 579 (1981).

685 ²³ W. S. Chang, M. Shanthi, K. K. Rajan, L. C. Lim, F. T. Wang, C. T. Tseng, C. S. Tu, P.
686 Yang, and H. O. Moser, *Journal of Applied Physics* **101**, 124104 (2007).

687 ²⁴ H. Cao, F. M. Bai, N. G. Wang, J. F. Li, D. Viehland, G. Y. Xu, and G. Shirane, *Physical*
688 *Review B* **72**, 064104 (2005).

689 ²⁵ G. Y. Xu, H. Hiraka, G. Shirane, and K. Ohwada, *Applied Physics Letters* **84**, 3975 (2004).

690 ²⁶ G. Y. Xu, D. Viehland, J. F. Li, P. M. Gehring, and G. Shirane, *Physical Review B* **68**,
691 212410 (2003).

692 ²⁷ W. Ge, C. P. Devreugd, D. Phelan, Q. Zhang, M. Ahart, J. Li, H. Luo, L. A. Boatner, D.
693 Viehland, and P. M. Gehring, *Physical Review B* **88**, 174115 (2013).

694 ²⁸ K. H. Conlon, H. Luo, D. Viehland, J. F. Li, T. Whan, J. H. Fox, C. Stock, and G. Shirane,
695 *Physical review B* **70**, 172204 (2004).

696 ²⁹ C. Luo, Y. Wang, Z. Wang, W. Ge, J. Li, H. Luo, and D. Viehland, *Applied Physics Letters*
697 **105**, 232901 (2014).

698 ³⁰ P. M. Gehring, W. Chen, Z. G. Ye, and G. Shirane, *Journal of Physics-Condensed Matter*
699 **16**, 7113 (2004).

700 ³¹ A. Lebon, H. Dammak, G. Calvarin, and I. O. Ahmedou, *Journal of Physics-Condensed*
701 *Matter* **14**, 7035 (2002).

702 ³² F. M. Bai, N. G. Wang, J. F. Li, D. Viehland, P. M. Gehring, G. Y. Xu, and G. Shirane,
703 *Journal of Applied Physics* **96**, 1620 (2004).

704 ³³ H. Cao, J. Li, and D. Viehland, *Journal of Applied Physics* **100**, 034110 (2006).

705 ³⁴ G. Xu, P. M. Gehring, C. Stock, and K. Conlon, *Phase Transitions* **79**, 135 (2006).

706 ³⁵ N. Domingo, N. Bagues, J. Santiso, and G. Catalan, *Physical Review B* **91**, 094111 (2015).

707 ³⁶ K. Ohwada, K. Hirota, P. W. Rehrig, P. M. Gehring, B. Noheda, Y. Fujii, S. E. E. Park, and
708 G. Shirane, *Journal of the Physical Society of Japan* **70**, 2778 (2001).

709 ³⁷ H. Cao, J.-f. Li, and D. Viehland, *Journal of Applied Physics* **100**, 084102 (2006).

710 ³⁸ Chrosch Jutta and E. K. H. Salje, *Journal of Physics: Condensed Matter* **10**, 2817 (1998).

711 ³⁹ E. K. H. Salje, M. Alexe, S. Kustov, M. C. Weber, J. Schiemer, G. F. Nataf, and J. Kreisel,
712 *Scientific Reports* **6**, 27193 (2016).

713 ⁴⁰ P. M. Gehring, K. Ohwada, and G. Shirane, *Physical Review B* **70**, 014110 (2004).

714 ⁴¹ P. Gao, H. J. Liu, Y. L. Huang, Y. H. Chu, R. Ishikawa, B. Feng, Y. Jiang, N. Shibata, E. G.
715 Wang, and Y. Ikuhara, *Nature Communications* **7**, 11318 (2016).

716 ⁴² H. You and Q. M. Zhang, *Physical Review Letters* **79**, 3950 (1997).

717 ⁴³ G. Y. Xu, P. M. Gehring, and G. Shirane, *Physical Review B* **72**, 214106 (2005).

718 ⁴⁴ G. Y. Xu, Z. Zhong, Y. Bing, Z. G. Ye, and G. Shirane, *Nature Materials* **5**, 134 (2006).

719 ⁴⁵ G. Y. Xu, Z. Zhong, Y. Bing, Z. G. Ye, C. Stock, and G. Shirane, *Physical Review B* **67**,
720 104102 (2003).

721 ⁴⁶ D. Viehland, *Journal of Applied Physics* **88**, 4794 (2000).

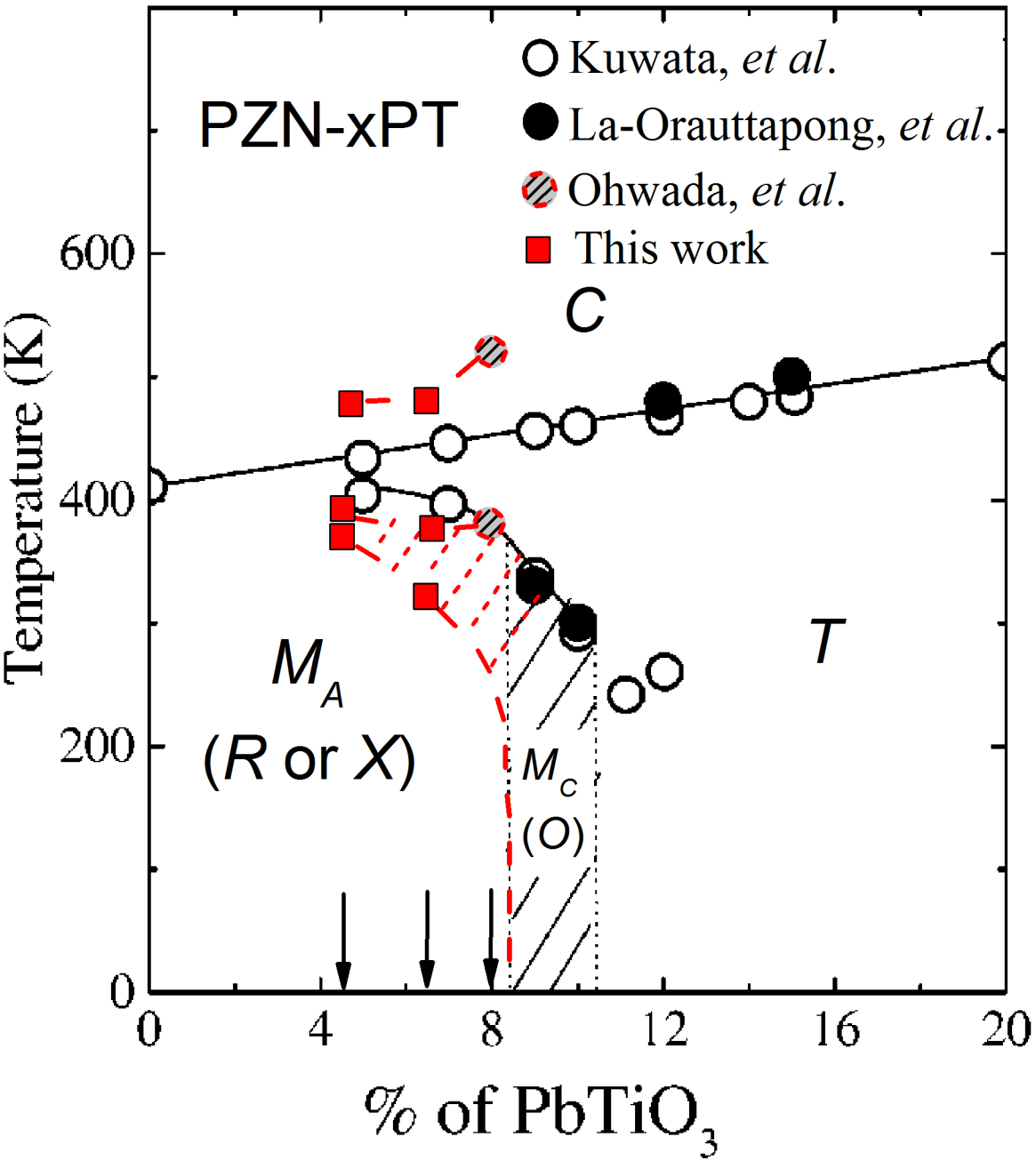
722 ⁴⁷ Y. M. Jin, Y. U. Wang, A. G. Khachatryan, J. F. Li, and D. Viehland, *Physical Review*
723 *Letters* **91**, 197601 (2003).

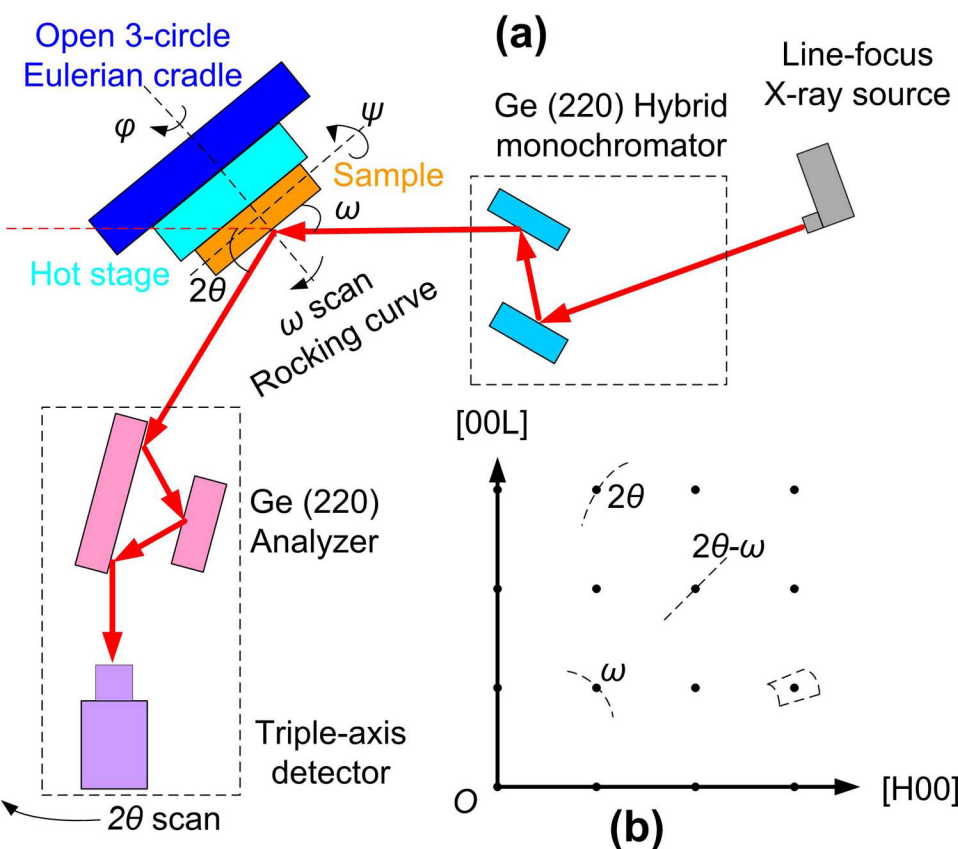
724 ⁴⁸ Y. U. Wang, *Physical Review B* **74**, 104109 (2006).

725 ⁴⁹ Y. U. Wang, *Physical Review B* **73**, 014113 (2006).

726 ⁵⁰ D. D. Viehland and E. K. H. Salje, *Advances in Physics* **63**, 267 (2014).

727





PZN-4.5PT, FC, $E=1\text{kV/cm}$

(a) (002)

(b) (200)

(c) (220) 390 K

(d)

(e)

(f) 380 K

(h)

(i)

(j) 300 K

PZN-6.5PT, FC, $E=1\text{kV/cm}$

(a) (002)

(b) (200)

(c) (220)

370 K

(d)

(e)

(f)

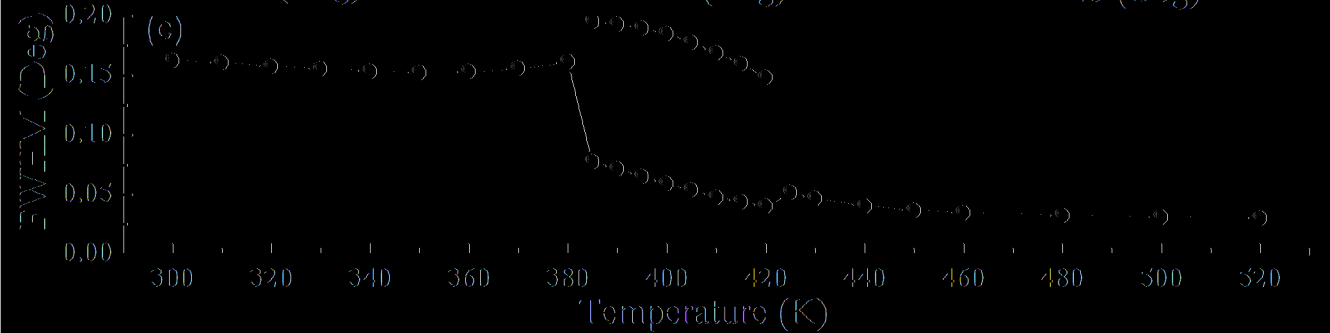
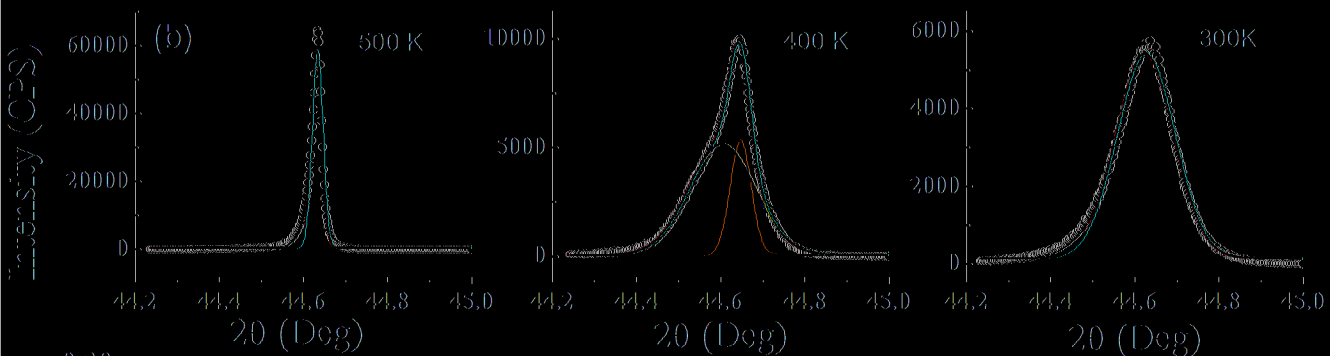
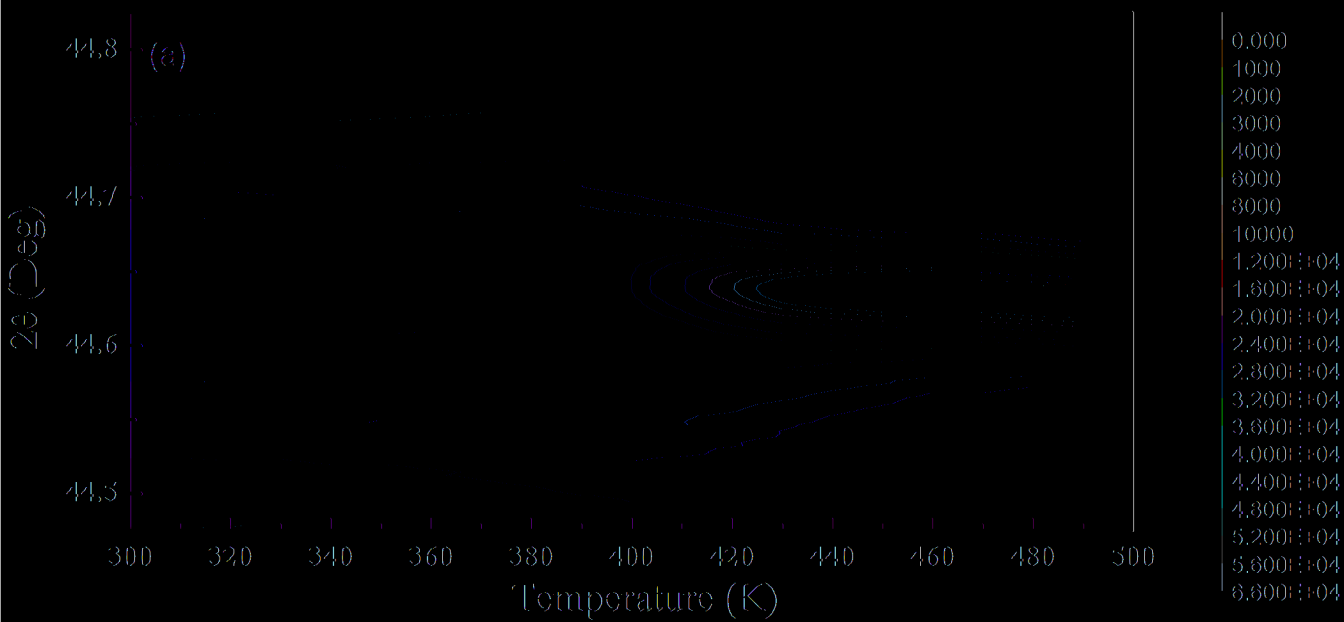
350 K

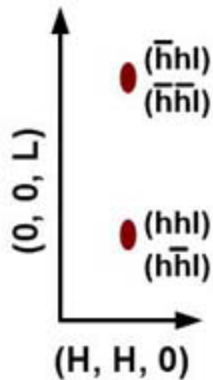
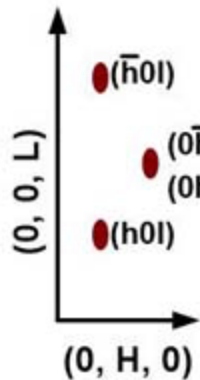
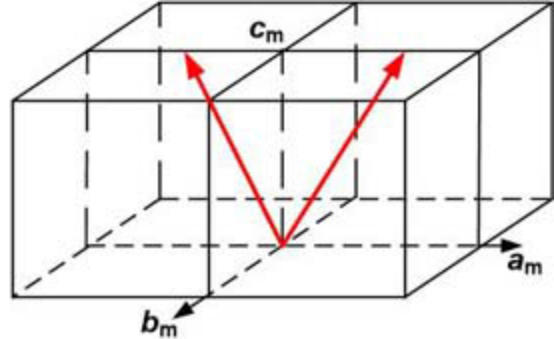
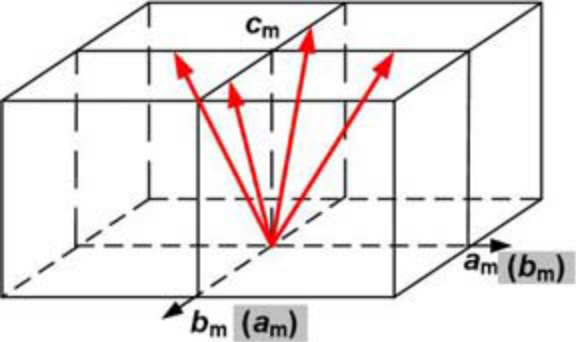
(h)

(i)

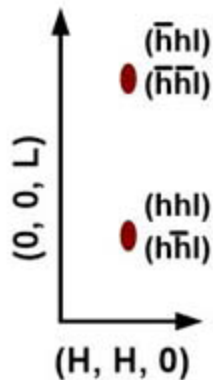
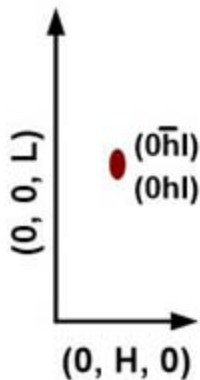
(j)

300 K





(a)



(b)